Channel interactions in the Ba $6d_j nl_{j'}$ autoionizing series for $l=2$, 3, and 4

R. R. Jones, Panming Fu, and T. F. Gallagher
Physics Department, University of Virginia, Charlottesville, Virginia 22901
(Received 1 October 1990)

We have used two-photon excitation of Ba $6snl$ Rydberg states to create Ba $6d_jnl$ autoionizing states. The excitation of the initial Rydberg states is performed using two, three, or four tunable dye lasers for $l=2$, 3, and 4 respectively. We have used very efficient laser pumping schemes for population of the $6snf$ and $6sng$ series. The $6d_jnl$ states exhibit a wide range of interseries interaction from large to negligible channel couplings. Furthermore, the quantum defects of all of the series have a pronounced energy dependence even in the absence of any coupling to other $6d_j$ core channels. The perturbing series that is the source of the energy variation of the quantum defects is believed to belong to one or more $4f_{j'}$ core configurations. Each $6dnl$ series has been fit using a multiconfiguration quantum-defect theory model, and the results of the fits are generally in good agreement with the observed spectra.

PACS number(s): 32.80.Dz

INTRODUCTION

In recent years there has been a great deal of experimental and theoretical interest in doubly excited states of alkaline-earth atoms [1–5]. All the alkaline-earth-metal atoms have a closed s^2 valence shell surrounding a highly bound doubly charged core. For over a decade most of the experimental investigations of autoionizing states in these atoms have been performed using tunable dye lasers in conjunction with the isolated core excitation (ICE) technique [1]. In this scheme one of the valence electrons is excited to a high-lying Rydberg state that spends most of its orbit time at a large radius, near its classical outer turning point. The autoionizing state is then created by exciting the inner or core electron to an excited state of the ion. Until very recently, the majority of the autoionizing alkaline-earth-metal-atom levels studied have been those where the core electron is excited to the first p state above the ionic ground state.

Although there have been a few studies of other core configurations in Ba [6,7] and Ca [8], the only doubly excited core configuration where a systematic study of all of the angular-momentum series of the outer electron have been observed is the Ba $6pnl$ configuration [2,3,9,10]. The Ba $5dnl$ states have also been populated for values of $l<6$ [11–13] but these series are usually not excited using an ICE. As experimentalists strive to populate more energetic core states, it is important that more than one outer electron configuration is observed. These systematic measurements are necessary so that we may acquire a better understanding of valence electron correlation as the excitation energy of the electron pair approaches the second ionization limit.

Here we report a detailed study of the Ba $6d_jnl_{j'}$ for $l=2$, 3, and 4. The $6d_{5/2}$ nd $J=4$ autoionizing series has been studied previously by Kachru *et al.* [14]. That investigation, like the one discussed here, also used a nonresonant two-photon excitation scheme. We have improved the signal-to-noise ratio of the previous study significantly and we are able to excite the series converging to both $6d_j$ fine-structure components. We also report the first observation of $6d_jns$ $J=2$, $6d_jnf_{j'}$ $J=3,5$, and $6d_jng_{j'}$ $J=5,6$ levels.

The $6dnl$ series were populated using two-photon core excitation from $6snl$ Rydberg states. We have used a standard two-step excitation of the $6sns$ and $6snd$ Rydberg states from the $6s^2$ ground state using an intermediate $6s6p\ ^1P_1$ level. The $6snf$ and $6sng$ Rydberg states were produced using three or four lasers, respectively, in conjunction with a combined laser photon absorption and stimulated emission excitation scheme. The technique will be discussed in the forthcoming experimental section.

The $6d_{3/2}nd_j$ $J=4$ and $6d_{5/2}nd_j$ $J=4$ series have been studied in detail for values of n ranging from 20 to 50. Specifically, we have measured both energy level positions and autoionization rates. We observe virtually no interaction between the two core configurations. We have fit the observed data using a two-channel quantum-defect theory (QDT) model for each of the core levels, a procedure which reproduces the spectra extremely well.

The $6d_{3/2}nf_{j'}$ states have been observed for $n=22-31$, and we have studied the $6d_{5/2}nf_{j'}$ states for $n=19-29$. We observe no correlation between the $6d_{3/2}$ and $6d_{5/2}$ core configuration as is the case for the nd states. We have fit the $6d_{5/2}nf_{j'}$ $J=5$ series using a four-channel QDT model and the $6d_{3/2}nf_{7/2}$ $J=5$ series using a two-channel model.

The $6d_jng_{j'}$ series show a large interseries interaction in contrast to the nd and nf states. We have studied the series converging to both fine-structure limits for values of n ranging from 13 to 30. We have fit the observed spectra using a ten-channel, energy-dependent QDT model. By energy dependent we mean that we have allowed the quantum defects and bound and continuum channel interactions to vary linearly with the binding energy of the outer electron. In general, the theoretical fits reproduce the data extremely well for all of the series studied.

The $6d_jns$ $J=2$ series have also been observed for $19<n<28$. The spectra for these series are extremely

complicated, indicating strong interseries interactions between $6d_{3/2}ns$ and $6d_{5/2}ns$ channels. Due to the noise level of the $6dns$ data and the complexity of the spectra, no theoretical fits were performed for these series.

EXPERIMENTAL PROCEDURE

For the population of $6dns$ and $6dnd$ states, the laser scheme is nearly identical to those discussed previously. First, two Hänsch-type [15] Nd:YAG (where YAG represents yttrium aluminum garnet) laser-pumped, pulsed dye lasers are used to excite ground-state Ba atoms to a $6sns$ or $6snd$ Rydberg state via the $6s6p\ ^1P_1$ intermediate level. The energy levels of these neutral levels have been measured previously [16,17]. The first dye laser has a pulse energy approximately equal to 50 μJ. The second laser, which is amplified, has a pulse energy of $\simeq 1$ mJ. A commercial dye laser which is pumped using an excimer laser is used to drive the isolated-core two-photon transition from any of the $6snl$ to a $6d_jnl$ state as shown in Fig. 1(a).

For the population of $6snf$ and $6sng$ states we use the laser excitation scheme shown in Fig. 1(b), in which three or four Hansch [15] dye lasers are used to create the initial Rydberg state. First, we populate the $5d6p\ ^3P_1$ level at 24 192.06 cm^{-1} [18]. Next, we use a laser whose frequency matches the $6s5d\ ^3D_2-5d6p\ ^3P_1$ energy interval [18] at 14 976.54 cm^{-1} to stimulate photon emission from atoms in the $5d6p\ ^3P_1$ level and transfer population to the $6s5d\ ^3D_2$ metastable state. Since we are able to saturate both transitions with very modest laser power approximately equal to 100 μJ, this two-laser pumping process is extremely efficient for packing the neutral Ba population in a $6s5d$ metastable state. Other mechanisms which have been used to transfer population to the $6s5d$ metastable are radiative decay from the $6s6p\ ^1P_1$ (less than 5% efficiency) or electron excitation in a spark gap. Our technique not only improves the efficiency of the transfer but also allows us to select the values of total angular momentum, J, and its projection on the z axis, M, which characterize the final state.

For excitation of $6nsf$ states, we use a single ultraviolet photon from a frequency-doubled dye laser to excite a member of the $6snf\ ^3F_3$ series from the $6s5d\ ^3D_2$ state. This dye laser has a frequency approximately equal to 16 000 cm^{-1} and a pulse energy approximately equal to 15 mJ before frequency doubling in a potassium dihydrogen phosphate (KDP) crystal. The frequency-doubled light has an energy approximately equal to 2 mJ. The energy positions and characteristics of the $6snf$ series have been studied in detail by Post *et al.* [19]. This series is strongly perturbed by the $5d8p$ and $5d4f$ configurations and the classification of the states in terms of LS coupling has only very limited validity. The classification of the $6snf$ series will be discussed in detail in the theoretical sections.

When $6sng$ states are populated we first drive the $6s5d\ ^3D_2-5d6p\ ^3D_3$ transition using a third dye laser before the final excitation from $5d6p\ ^3D_3$ to $6sng\ ^3G_4$. The third laser has a pulse energy of $\simeq 100$ μJ and has its frequency fixed at 15 764.34 cm^{-1} [18] while the fourth dye laser has a pulse energy of $\simeq 5$ mJ and a frequency of $\simeq 17\,000$ cm^{-1}. The frequency of the fourth laser is tuned so as to excite a given member of the $6sng$ series whose energies have been tabulated previously [20]. The $6sng$ states are actually excited through the $5d7d$ character which is mixed into the series. The presence of these perturbers prevents a uniform description of the series in

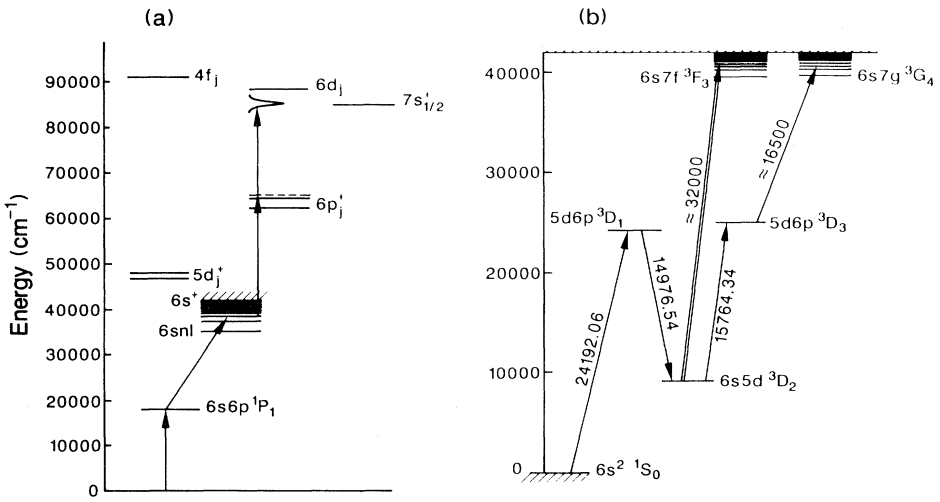

FIG. 1. (a) Diagram of the laser scheme for excitation of $6dns$ and $6dnd$ states. Two lasers excite a $6sns$ or $6snd$ state via the $6s6p\ ^1P_1$ intermediate states. The final laser drives a two-photon $6s$-$6d_j$ core transition. (b) Schematic of the laser scheme used for population of $6snf$ and $6sng$ Rydberg states. The first laser excites ground-state atoms to the $5d6p\ ^3D_1$ level which then undergoes stimulated emission to the $6s5d\ ^3D_2$ state using the second laser as a stimulus. The final transition to the Rydberg state is then performed using a single step for the $6snf$ states or using two steps with an intermediate $5d6p\ ^3D_3$ level.

terms of standard LS or j-j coupling. The effects of the nonuniform coupling have a profound effect on the appearance of the final states which we excite.

In all cases, the final laser beam which drives the $6snl$ to $6dnl$ transition is sent through a telescope which allows us to change the beam diameter and thereby vary the intensity of the laser in the interaction region. The power of the third laser is varied, for reasons which will be discussed later, yielding pulse energies between $\simeq 100$ and 10 mJ. This laser is sent into a vacuum chamber with a background pressure of 10^{-7} Torr, antiparallel to the other lasers and perpendicular to the effusive Ba beam which originates in a resistively heated oven. The lasers and Ba atoms interact between a set of aluminum-field plates. After the atoms autoionize we measure the Ba^+ or electron current from a microchannel plate detector as a function of third laser frequency. For the $6dns$ and $6dnd$ series, we measure ion current and for the $6dnf$ and $6dng$ series we collect electrons. The temporal pulse widths of the dye lasers are $\simeq 8$ ns and the pump lasers are fired at a 20-Hz repetition rate.

EXPERIMENTAL RESULTS

Different laser polarizations were used in order to select different final-state angular momenta in the excitation of all the levels studied. With linear polarization, the allowed final states are $6dns$, $J=2$; $6dnd$, $J=2,4$; $6dnf$, $J=3,5$; and $6dng$, $J=4,6$. However, only $6dnd$, $J=4$; $6dnf$, $J=5$; and $6dng$, $J=6$ are allowed if all of the lasers are circularly polarized so as to allow $\Delta M=+1$ transitions only. For the $6dnd$ series, this criterion is satisfied if all three lasers are circularly polarized in the same sense. However, for the $6dnf$ and $6dng$ excitations, the second laser must be circularly polarized in a sense opposite to that of the other lasers because this laser photon stimulates emission of a photon rather than being absorbed.

No differences in the final spectra were observed with linear or circular polarization for the $6dnd$ and $6dnf$ series indicating that the levels with different values of J are degenerate. For the $6dng$ series, data were also taken with the second laser circularly polarized in the same sense as the other lasers, thereby performing a $\Delta M=-1$ transition. This allows approximately 60% of the $6d_{3/2}ng$ population to be in a $J=5$ state with less than 35% in the $J=6$ level and nearly 35% of the $6d_{5/2}ng$ population is allowed to have $J=5$ with only 60% possessing $J=6$. Again, no difference was observed in the final spectra suggesting that the $6dngJ=5$ and 6 levels are degenerate.

$6d_j nd_{j'}$ $J=4$ SERIES

Figure 2 shows a scan of the third laser frequency showing the transition from the bound $6s30d$ state to the $6d_j nd$ $J=4$ states of $n\simeq 30$. The excitation of the series converging to both the $6d$ fine-structure components can be clearly seen. For this scan the third laser power is high enough so that the central features for states converging to both the $6d_{3/2}$ and $6d_{5/2}$ limits are depletion

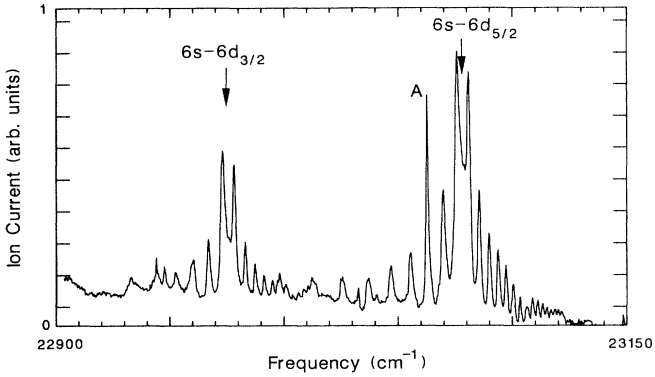

FIG. 2. Spectra obtained by scanning the third-laser frequency after the initial excitation of a $6s30d$ Rydberg state. The positions of the two-photon ion transitions $6s$-$6d_{3/2}$ and $6d$-$6d_{5/2}$ are labeled. The feature labeled A is a neutral Ba frequency marker line at 23 062.06 cm^{-1}.

broadened [21]. This broadening increases the relative amplitudes between the satellite structures and the central peaks. Also note the large sloping background signal due to single photon excitation of the $6p_{3/2}\epsilon l$ continuum.

Figure 2 shows spectra which are characteristic of an excitation from a bound state with quantum defect δ to an autoionizing state with quantum defect $\delta'=\delta+\frac{1}{2}$ [3]. The seemingly complicated structure is easily explained using a two-channel QDT model. In the ICE approximation the cross section for excitation of an autoionizing series is proportional to the square of the overlap integral for the outer electron multiplied by the spectral density of the final autoionizing states [3]. The basic structure seen here arises because the central maximum of the overlap integral is centered between two maxima in the spectral density of the final state. The subsidiary maxima in the overlap integral, on the other hand, coincide with the maxima in the spectral density of the autoionizing series. In Ref. [3] a number of plots are presented which explicitly show the dependence of the final-state spectra on the difference between the quantum defects of the initial and final outer electron states in an ICE.

Since the satellite features exhibit essentially Lorentzian profiles, their positions and widths may be used to directly determine the quantum defects and autoionization rates of the series of interest. This would not be the case if the quantum defects of the initial- and final-state series differed by more than $\simeq 0.6$ or less than $\simeq 0.4$. In principle, the satellite levels, by virtue of their Lorentzian profiles, should yield the correct quantum defects and rates. The central maxima, on the other hand, may be significantly altered by the overlap integral. Thus, we use the satellite features to determine the quantum defects and autoionization rates.

Unfortunately, the amplitude of the first satellite level is approximately 10% of the amplitude of the central features giving a greatly reduced signal-to-noise ratio. This ratio can be improved, however, by increasing the intensity of the third laser. This increased intensity will depletion broaden the largest features, but the satellite

states should not broaden if their amplitudes remain less than approximately half of the amplitude of the central features. Therefore, we use high-intensity third-laser scans in order to study the satellite features in detail. In Fig. 3(a) we show a high-intensity third-laser scan over $6d_{3/2}nd$ levels excited from a $6s35d$, state and in Fig. 3(b) we show an analogous scan over $6d_{5/2}nd$ states from an initially populated $6s32d$ Rydberg level. Scans similar to those shown in Fig. 3 were used to determine the quantum defects and autoionization rates of the respective series.

We also made several scans of the third-laser frequency over a range of states with $27 < n < 38$ using much lower laser power. Figures 4(a) and 4(b) show excitation spectra from $6s30d$ and $6s33d$ initial states, respectively. These spectra exhibit no saturation broadening. The quantum defects and autoionization rates determined from these levels were also measured. Next, a comparison was made between the quantum defects and the autoionization rates which were obtained from the saturated and nonsaturated laser scans. As expected, the quantum defects obtained from the two types of spectra agree very well with each other. On the other hand, the widths determined using the high- and low-power scans differed by as much as a factor of 2 for some levels.

The origin in the discrepancy lies in our assumption that our third-laser beam has a constant intensity throughout the beam profile. For a uniform beam intensity, each atom in the laser beam sees the same number of photons, and therefore, each volume element of $6snd$ Rydberg atoms in the laser beam is depleted by the same level. Furthermore, for a beam of uniform intensity, all thoroughly saturated features have the same peak amplitude. By increasing the scanning range of the third laser, for a given $6snl$ Rydberg level, we may examine the single-photon excitation to the $6p_{3/2}nd$ series as well as the two-photon excitation to the $6dnd$ states. If the power of the laser is increased so that the $6dnd$ profiles are severely broadened, then the peak amplitude of the $6p_{3/2}nd$ autoionizing state should be equal to the amplitude of the $6dnd$ states. This is not the case, and we observe that the ratio of the peak amplitude of the $6p_{3/2}nd$ structure to that of the $6d_{5/2}nd$ structure is nearly 20.

This experimental evidence shows that the actual profile of our laser beam is certainly not of uniform intensity. Thus, the volume of excited atoms may be significantly depleted at the center of the beam profile but not in the wings. Hence, the amplitude of a given feature never attains a maximum value, but instead, it may continue to increase as more atoms are excited by the spatial

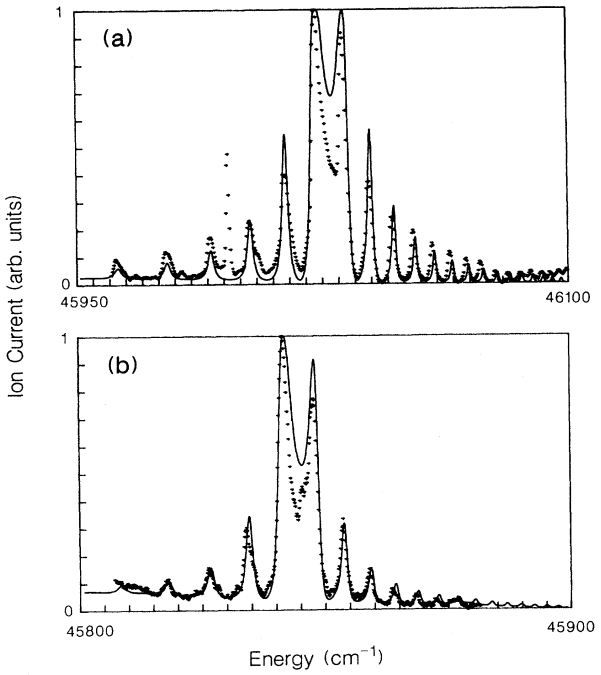

FIG. 3. Frequency scan of the third laser after the initial excitation of a $6snd$ Rydberg level. (a) shows excitation from $6s35d$ exhibiting several $6d_{3/2}nd$ levels and (b) shows excitation from $6s32d$ exhibiting several $6d_{5/2}nd$ states. These spectra are intentionally depletion broadened to increase the amplitude of the satellite states. The smooth curve is the theoretical fit described in the analysis section. The energy scale is relative to the first ionization limit.

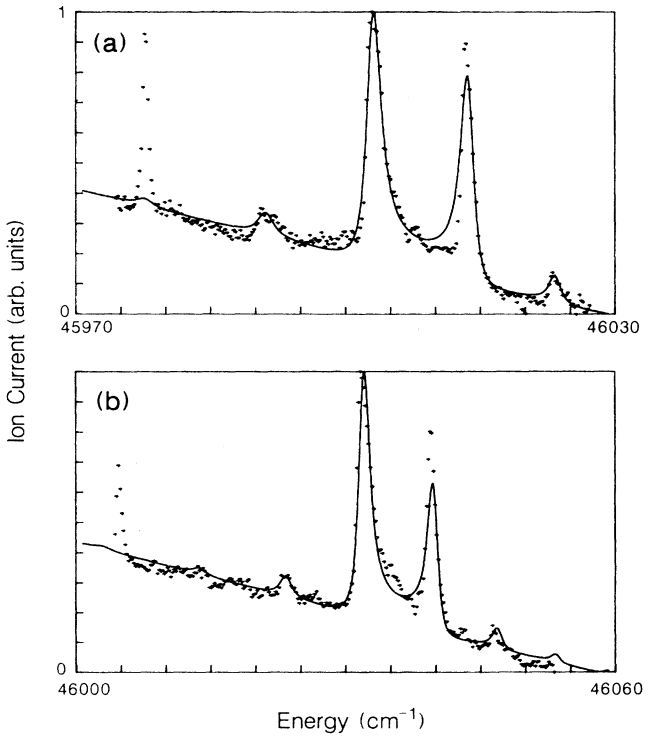

FIG. 4. Low power scan of the third laser after the excitation of a $6snd$ level for (a) $n = 30$ and (b) $n = 33$. Note the large sloping background due to single photon excitation of the $6p\epsilon l$ continua. The energy scale is relative to the first ionization limit. The smooth curve is a theoretical fit to the data as discussed in the analysis section.

wings of the laser pulse. The major contribution to the satellite features in our saturated spectra obviously originates in a spatial region where the initial Rydberg state population has been depleted and these features are, therefore, broadened. Hence, the experimental widths which are plotted in Fig. 5(a) are those derived from the nonsaturated scans.

For the higher n levels, the widths of the observed autoionizing states are within a factor of 3 of our laser linewidth of $\simeq 0.35$ cm^{-1}. The value for the laser linewidth is determined using a single-photon neutral Ba resonance which appears near the $6d_{5/2}$ ion line. This resonance is the quadrupole transition, $6s^2\,{}^1S_0 - 5d^2\,{}^1D_2$ at 23 062.06 cm^{-1} [18]. Although this transition should have a small excitation amplitude, the absorption of a second photon at this frequency places the Ba atom only 1.2 cm^{-1} below a Ba $5d_{5/2}nd$, $J=2$ level at 46 125.46 cm^{-1} [11]. Therefore, due to the non-negligible width of the $5dnd$ autoionizing state, the light of frequency 23 062.06 cm^{-1} may create Ba^+ ions through a resonant two-photon process. In any case, the laser linewidth is deconvoluted from the observed Voight profiles in the ion spectrum, and the rates reported here are the adjusted widths.

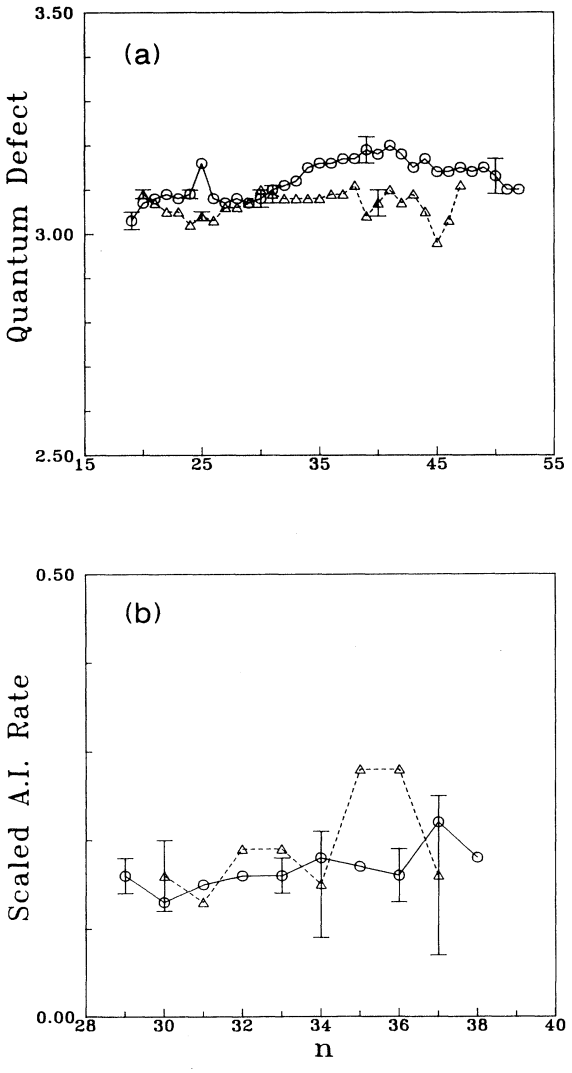

FIG. 5. (a) Experimental scaled autoionization rates in atomic units, $\nu^3\Gamma$, for the $6d_{3/2}nd$, $J=4$ (△) and $6d_{5/2}nd$, $J=4$ (○) autoionizing series plotted vs n. (b) Experimental quantum defects for the $6d_{3/2}nd$, $J=4$ (△) and $6d_{5/2}nd$ (○), $J=4$ autoionizing series plotted vs n.

The measured autoionization rates scale as ν^{-3} as expected, where ν is the effective quantum number of the outer electron. The average scaled autoionization rates $\nu^3\Gamma$ for the two series are

$$\nu^3\Gamma_{6d_{3/2}nd} = 0.19 \pm 0.02$$

and

$$\nu^3\Gamma_{6d_{5/2}nd} = 0.16 \pm 0.01$$

in a.u.

The quantum defects obtained from the saturated scans are still valid since the observed features are broadened symmetrically. The quantum defects shown in Fig. 5(b) are the averages of the satellite peak positions from several third-laser frequency scans. Often, 20 or more satellite states were excited for a given initial state. Therefore, as many as ten energy position measurements were averaged to determine the quantum defects for each of the $6d_j nd$ states. The measured quantum defects have average values of

$$\delta_{6d_{3/2}nd} = 3.07 \pm 0.01$$

and

$$\delta_{6d_{5/2}nd} = 3.12 \pm 0.01\ .$$

The experimental values for the scaled autoionization rates and quantum defects of the $6d_{5/2}nd$ series are in good agreement with those previously reported [14].

$6d_j nf_{j'}$, $J=5$ SERIES

All of the $6d_j nf_{j'}$ spectra were taken by scanning the frequency of the final laser near the $6s6d_j$ two-photon transition line at an intensity level such that the observed profiles exhibited no saturation broadening [21]. The $6d_{3/2}nf_{7/2}$ levels are quite broad and have widths which are approximately one-third of the spacing between adjacent n levels. The members of this series for $21 < n < 32$ show no indication of any interaction with the $6d_{5/2}nf_{j'}$ levels. Since there is only one $6d_{3/2}nf$ $J=5$ channel, the experimental energy positions and widths were determined by fitting the data to a single Lorentzian. The autoionization rates Γ are taken as the FWHM of the profiles we observe. The experimental quantum defects and scaled autoionization rates, $\nu^3\Gamma$ (ν is the effective quantum number) are plotted versus a principle quantum number in Figs. 6(a) and 6(b), respectively. The average values for the quantum defects and scaled autoionization rates are

$\delta_{6d_{3/2}nf_{7/2}}=1.00$,

$\nu^3\Gamma_{6d_{3/2}nf_{7/2}}=0.30$

in a.u.

The $6d_{5/2}nf_{5/2}$, $J=5$ and $6d_{5/2}nf_{7/2}$, $J=5$ states are slightly longer lived than the $6d_{3/2}nf_{7/2}$ states as evidenced by their narrower profiles. The profiles we observe clearly show two features which appear regularly for $18<n<30$ indicating little or no interaction with any other channels. Since there are two allowed channels converging to the $6d_{5/2}$ limit, the data here have been fit to the sum of two Lorentzians. The experimental quantum defects and scaled autoionization rates of the two observed series are plotted in Figs. 7(a) and 7(b) respectively. The average values obtained for the quantum defects and scaled autoionization rates for the two series are

$\delta_{6d_{5/2}nf_{5/2}}=1.12$,

$\delta_{6d_{5/2}nf_{7/2}}=0.98$,

$\nu^3\Gamma_{6d_{5/2}nf_{5/2}}=0.17$,

$\nu^3\Gamma_{6d_{5/2}nf_{7/2}}=0.12$,

where the scaled rates are given in a.u.

There are two obvious features of the $6dnf$ spectrum which should be noted. First, the quantum defects of all of the observed series increase slightly with increasing energy. Second, the relative strengths of the two different channels converging to the $6d_{5/2}$ ion limit vary from state to state indicating a nonconstant admixture of the

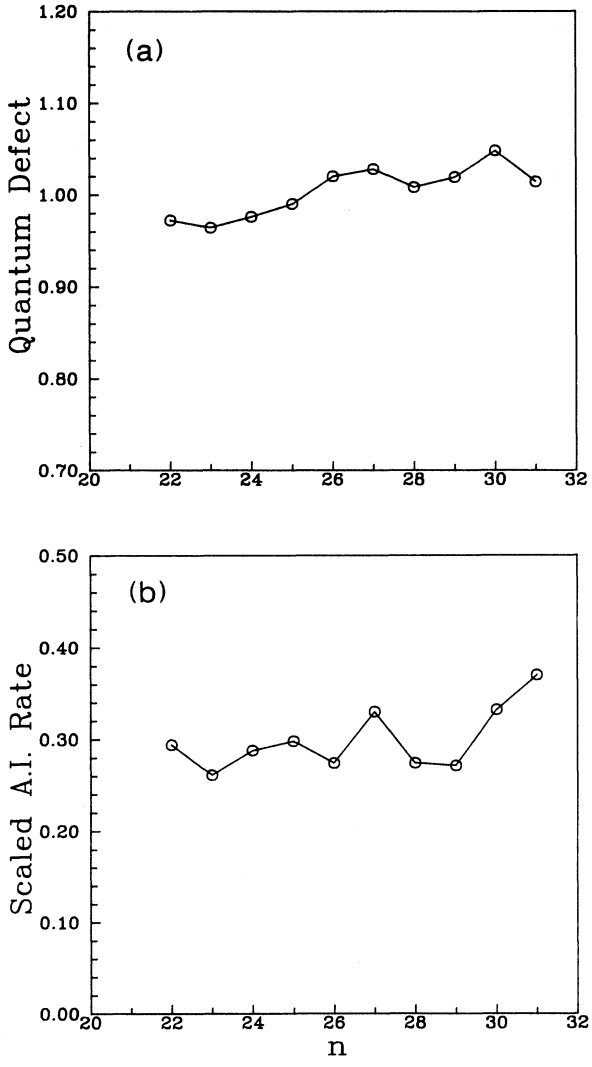

FIG. 6. (a) Experimental quantum defects and (b) scaled autoionization rates, $\nu^3\Gamma$, for the $6d_{3/2}nf_{5/2}$, $J=5$ autoionizing series plotted vs n. The rates are reported in a.u.

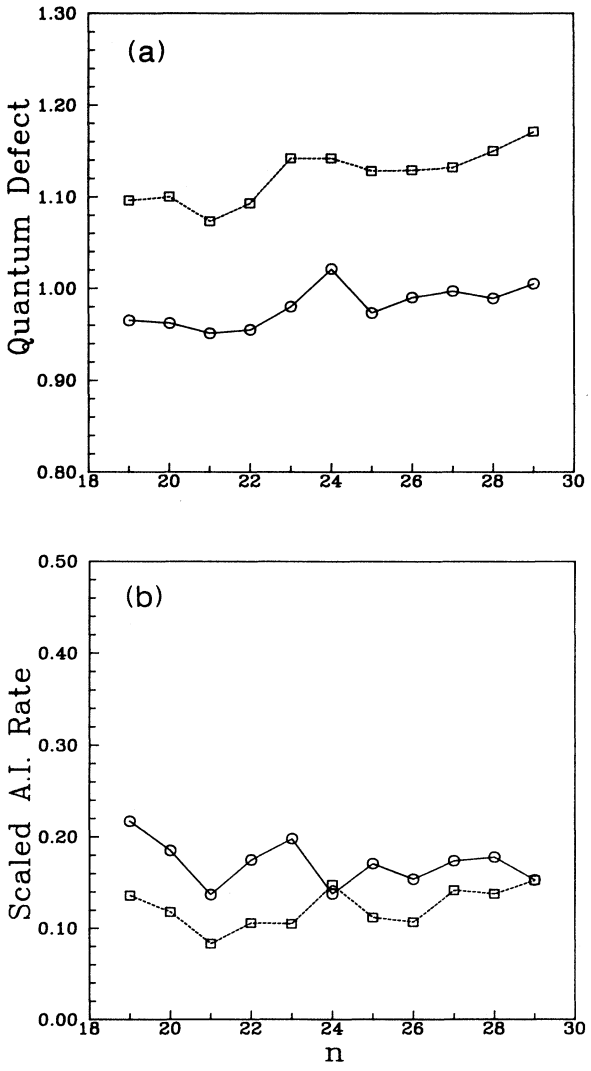

FIG. 7. (a) Experimental quantum defects for the (□) $6d_{5/2}nf_{5/2}$, $J=5$ and (○) $6d_{5/2}nf_{7/2}$, $J=5$ autoionizing series plotted vs n. (b) Scaled autoionization rates, $\nu^3\Gamma$, for the (○) $6d_{5/2}nf_{5/2}$, $J=5$ and (□) $6d_{5/2}nf_{7/2}$, $J=5$ autoionizing series in a.u. plotted vs n.

two allowed j-j coupled channels in the $6snf$ $J=3$ initial states. This effect has been observed previously in the study of the $6pnf$ series [9]. Both of these experimental observations will be discussed in more detail in the theoretical and discussion sections of this work.

$6d_j ng_{j'}$ $J=6$ SERIES

The $6dng$ series exhibit strong interseries interactions between levels converging to the different fine-structure component of the Ba^+ $6d$ ion limit. It is not surprising that strong couplings occur when we consider that the Ba^+ $6d_j$ fine-structure splitting is only 205 cm^{-1} [18]. Similar interferences have been observed in the Mg $3pnl$ levels [32] where the $3p_j$ fine-structure splitting is 92 cm^{-1} [18]. Some of the perturbations may also be due to coupling with even-parity $4f_j nl$ states which are strongly coupled to the $6d_j nl$ series. In any case, the observed profiles show no regular features to which we may assign quantum defects or autoionization rates. Therefore, in order to report the results of our experiments we simply show all of the spectra we observe as a function of final-state energy in Figs. 8–10. Figures 8(a), 9(a), and 10(a) show the series converging to the $6d_{5/2}$ ion limit and Figs. 9(d) and 10(d) show the series converging to the $6d_{3/2}$ limit.

Each of the major features in Figs. 8–10 are obtained from a different initial $6sng$ Rydberg state and the amplitudes are normalized to 1 individually. Obviously, the spectra are extremely complicated. The ten-channel QDT fit to the data is shown in parts (b) and (c) of the figures. The details of the energy-dependent model, which was used for the fit, will be discussed in the upcoming theoretical sections.

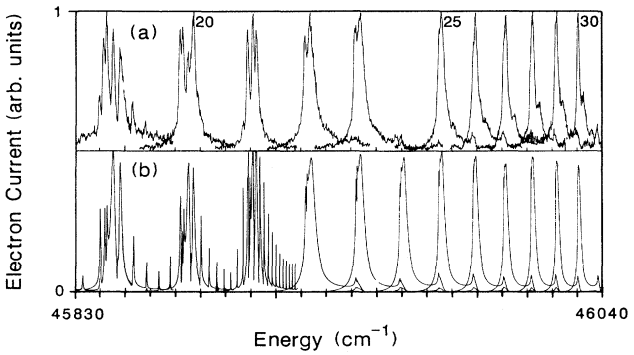

FIG. 8. (a) Experimental and (b) theoretical spectra for excitation of the $6d_{5/2}ng(i)$ $J=6$ autoionizing series shown as a function of final-state energy. Each of the main features was excited from a different initial $6sng$ state and the synthesized and experimental spectra are individually normalized to unity. The theoretical spectra are calculated using the ten-channel QDT model discussed in the text. Some of the sharp features in the synthesized spectra are washed out in the data due to instrumental broadenings on the order of 0.5 cm^{-1}. The energy scale is relative to the first ionization limit. The experimental data is not available for the $6d_{5/2}24g$ state due to difficulty in exciting the $6s24g$ state.

$6d_j ns$ SERIES

The excitation cross sections observed from initial $6sns$ levels are also significantly perturbed. The spectra obtained from different initial Rydberg states exhibit interferences which appear to be completely different from one level to the next as is the case with the $6dng$ series. This observation suggests that the interferences arise from interactions with series converging to different core limits. Interference effects originating from couplings to channels converging to the same Ba^+ limit should scale with increasing energy such that each n level has the same effective profile. Interactions between series converging to the different $6d_j$ fine-structure levels are believed to be the major cause of the interferences, since the energy spacings between the dips in the $6d_{5/2}ns$ spectra are of the same order as the spacings between adjacent $6d_j nl$ levels.

There is an enormous number of bound, even-parity $J=2$ levels which can conceivably interact with the $6d_j ns$ $J=2$ states. Fitting the experimental spectra to a set of multiconfiguration quantum-defect theory (MQDT) parameters would be extremely difficult and it is doubtful that a meaningful set of coupling parameters could be obtained. However, it has been shown that *ab initio* calculation can accurately reproduce autoionization spectra in alkaline-earth atoms [22,23]. Such calculations may be feasible for Ba. Therefore, we postpone any detailed

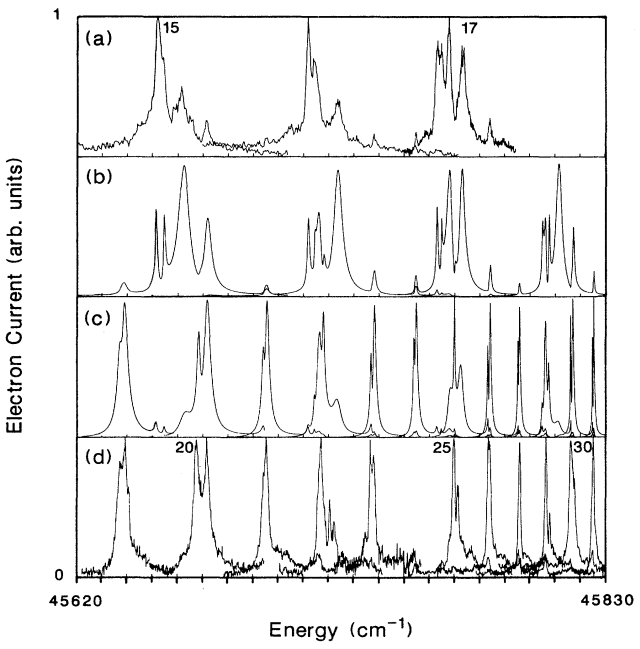

FIG. 9. (a) Experimental and (b) theoretical spectra for excitation of the $6d_{5/2}ng(i)$, $J=6$ series analogous to Fig. 8(c). Synthesized and (d) experimental spectra for excitation of the $6d_{3/2}ng(i)$, $J=6$ series. Data are not available for the $6d_{3/2}24g$ and $6d_{5/2}18g$ levels due to difficulty in exciting the $6s24g$ and $6s18g$ states. Each main feature was excited from a different initial Rydberg level and are normalized individual to unity. The energy scale shown is relative to the first ionization limit.

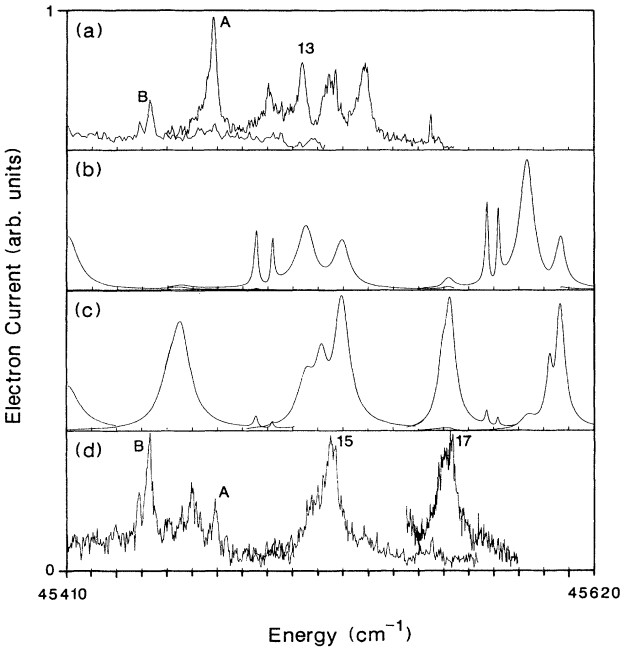

FIG. 10. (a) and (d) show experimental excitation of the $6d_{5/2}ng(i)$, $J=6$ and $6d_{3/2}ng(i)$ $J=6$ series, respectively, and (b) and (c) show the theoretical synthesized spectra of these series completely analogous to Fig. 9. Note the features which are labeled A and B which are believed to be $4fnl$ perturbers which are the source of the energy dependence of the MQDT parameters and quantum defects. Similar sharp features have been observed near $6d_{3/2}13g$ and $6d_{5/2}12g$.

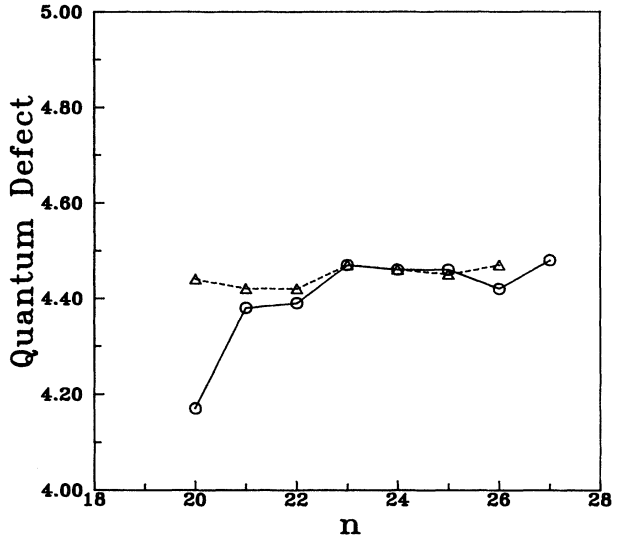

FIG. 11. Experimental quantum defects for the $6d_{3/2}ns$, $J=2$(○) and $6d_{5/2}ns$, $J=2$ (Δ) autoionizing series plotted vs n. The quantum defects for the perturbed levels were determined from the energy positions of the center of the largest feature in the experimental spectra.

analysis of the $6d_jns$ series until such calculations can be obtained.

Despite the large perturbations in the series, a plot of the measured quantum defects for the $6dns$ series is shown in Fig. 11. The quantum defects are derived from the energy positions of the centers of the main features in the spectra. No autoionization rates are reported for these series due to the interference effects.

ANALYSIS OF THE $6d_jnd$ $J=4$ SERIES

The single-photon, energy-dependent cross section for a one-electron excitation from an initial state $|1\rangle$ to a final state $|2\rangle$ can be written in atomic units as [24]

$$\sigma=4\pi^2\alpha\omega|\langle 1|r|2\rangle|^2\Omega(E_2)\ , \tag{1}$$

where ω is the photon frequency, α is the fine-structure constant, Ω represents the density of the final state, and r is the dipole operator which includes angular as well as radial terms. Using Eq. (1), we may write the cross section for a typical isolated core excitation [1] from a $6snl$ level to a $6pn'l'$ level in atomic units as

$$\sigma=\frac{4\pi^2\alpha\omega}{\nu_i^3}|\langle 6p|r|6s\rangle\langle n'l'|nl\rangle A(\nu)|^2\ , \tag{2}$$

where ω is the photon frequency, α is the fine-structure constant, ν_i is the effective quantum number of the initial Rydberg state, and $|A(\nu)|^2$ is the spectral density of the final autoionizing state. The factor of ν_i^3 appears in the denominator because the initial states are not energy normalized. The angular factors which arise due to the uncoupling of the two-electron angular momenta are implicitly included in r. In writing Eq. (2) we have implicitly assumed that a true isolated core transition has occurred. That is, we assume that direct excitation of the $6s\epsilon l''$ continua, which is degenerate with the $6pn'l'$ state is negligible. Equation (2) has been shown to reproduce observed cross sections over a variation of three orders of magnitude [25].

The rate at which the doubly excited states are produced by a pulsed laser is then given by

$$W=\frac{\sigma\Phi}{\tau}\ , \tag{3}$$

where Φ is the time-integrated photon flux in the laser pulse and τ is the temporal pulse width of the laser. Equation (3) assumes that the laser is a square pulse. However, from Fermi's golden rule, the rate at which a transition occurs between two levels, $|1\rangle$ and $|2\rangle$ which are coupled by a perturbation, $V(r)e^{i\omega t}$, can be written to first order as [24]

$$W_1=2\pi|\langle 1|V|2\rangle|^2\Omega(E_2)\ . \tag{4}$$

Equating Eqs. (3) and (4) and substituting Eq. (1) for σ, we arrive at an expression for the form of the perturbing potential in a one-photon excitation

$$|\langle 1|V|2\rangle|^2=\frac{2\pi\omega\alpha\Phi}{\tau}|\langle 1|r|2\rangle|^2\Omega(E_2)\ . \tag{5}$$

The two-photon excitation which is of interest here involves transitions through virtual intermediate states,

which lie in the continuum, to final higher-lying autoionizing states. Because the intermediate and final states lie in the continuum, we can express the rate for two-photon transitions from an initial state $|1\rangle$ to a final state $|2\rangle$ as [24]

$$W_2 = 2\pi \left| \int \frac{\langle 1|V|k\rangle \Omega(E_k) \langle k|V|2\rangle}{E_1 - E_k + \omega} dE_k \right|^2 \Omega(E_2) , \quad (6)$$

where $\Omega(E_k)$ and $\Omega(E_2)$ are the density-of-state functions for the intermediate and final levels, respectively.

Substituting Eq. (5) for the perturbing potentials in Eq. (6) and using Eq. (3) to relate the transition rate to the cross section, we easily obtain an expression for the two-photon cross section for excitation of state $|2\rangle$ from an initial state $|1\rangle$,

$$\sigma' = \frac{8\pi^3 \omega^2 \alpha^2 \Phi}{\tau} \times \left| \int \frac{\langle 1|r|k\rangle \Omega(E_k) \langle k|r|2\rangle}{E_1 - E_k + \omega} dE_k \right|^2 \Omega(E_2) . \quad (7)$$

In writing Eqs. (6) and (7), we have assumed that the intermediate states $|k\rangle$ are not coupled to any other states through some perturbation other than the laser. To include such effects we could add an imaginary part to the energy of the intermediate states in a somewhat *ad hoc* fashion. However, the strengths of the couplings to other states due to typical processes such as radiative decay or blackbody radiative redistribution are much smaller than the other couplings of interest and occur over much longer time scales. Thus, we ignore these complications. Of course, the process of autoionization is implicitly taken into account when we write the state $|k\rangle$ as an eigenstate of the two-electron system which contains both bound and continuum parts. In this representation, the eigenstates does not "decay" since the continuum part of the wave function is always present.

With these clarifications Eq. (7) can be readily generalized to express the two-photon ICE cross section for excitation of a $6d_j n'l'$ autoionizing state from a $6snl$ Rydberg state

$$\sigma' = \frac{16\pi^3 \omega^2 \alpha^2 \Phi}{\nu_i^3 \tau} \left| \int dE_{n''} \sum_{j''l''} \langle 6d_j|r|6p_{j'}\rangle \langle 6p_{j'}|r|6s\rangle \langle n'l'|n''l''\rangle |A_{n''l''}|^2 \frac{\langle n''l''|nl\rangle A_{n'l'}}{(E_{6s} - E_{6p_{j'}}) + (E_n - E_{n''}) + \omega} \right|^2 , \quad (8)$$

where $|A_n''l''|^2$ is the spectral density for the intermediate $n''l''$ Rydberg level and $|A_{n'l'}|^2$ is the spectral density for the final autoionizing state. Also note that we have inserted an extra factor of 2 in the cross-section formula to account for the possible absorption of photon 2 before photon 1.

Cooke and Cromer [26] have derived a simplified expression for the general two-photon ICE by performing the sum over the intermediate outer electron states in Eq. (8). The formula they obtain contains two terms. One term describes direct absorption of two photons with the outer electron shaking only to the final state. The second term describes a stepwise excitation through nearby intermediate autoionizing states. In our excitation scheme, there are no nearby intermediate autoionizing states since the first photon places the atom above the Ba^+, $6p_{3/2}$ limit. Thus, we only need to consider the first term in the Cooke and Cromer [26] cross-section formula, and Eq. (8) becomes

$$\sigma' = \frac{16\pi^3 \omega^2 \alpha^2 \Phi}{\nu_i^3 \tau} \left| \sum_{j'} \frac{r_{6d_j 6p_{j'}} r_{6p_{j'} 6s}}{\Delta_{j'}} \langle n'l'|nl\rangle A_{n'l'} \right|^2 , \quad (9)$$

where

$$\Delta_{j'} = E_{6s} - E_{6p_{j'}} + \omega .$$

Again, the radial matrix elements above implicitly contain all of the angular integrals involved in decoupling the individual electron's angular momentum and spin from the total angular momentum.

The time-integrated photon flux and laser pulse width are known approximately, and the expression for the overlap integral of the outer electron can be written in closed form as [25]

$$\langle \nu_i l|\nu l'\rangle = \delta_{l,l'} \frac{\sin\pi(\nu_i - \nu)}{\pi(W_i - W)} , \quad (10)$$

where ν_i and ν are the initial and final effective quantum numbers, l and l' are the initial and final angular-momentum quantum numbers, and W_i and W are the binding energies of the initial and final Rydberg states, respectively. We assume that there are no interactions between the allowed bound final-state channels. In this case, the spectral density for each of the allowed final states has contributions from one bound and one continuum channel only. Cooke and Cromer [27] have shown that, for one bound and one continuum channel, the bound-state spectral density has the simple form

$$|A_{n'l'}|^2 = R'^2 \frac{1 + \tan^2(\pi\nu')}{R'^4 + \tan^2(\pi\nu')} , \quad (11)$$

where R' is the coupling parameter which connects the bound and continuum channels and ν' is the effective quantum number of an energy position in the final-state spectrum added to the quantum defect of the bound autoionizing channel. It is easy to show that for values of $R' \ll 1$, the function in Eq. (11) exhibits profiles which are nearly Lorentzian and have FWHM's of

$$\Gamma=\frac{2R'^2}{\pi\nu^3} \tag{12}$$

in a.u. [27].

Using Eq. (9), the total cross section for two-photon excitation of $6dnd$ $J=4$ levels can be expressed as

$$\sigma'_T=\sigma'_{6d_{5/2}nd_{3/2}}+\sigma'_{6d_{5/2}nd_{5/2}}+\sigma'_{6d_{3/2}nd_{5/2}}\ , \tag{13}$$

which is just a sum over the allowed final states. Unfortunately, our spectra also show a nonconstant background due to a single-photon excitation of $6p_j\epsilon l$ continua. We must include a single-photon cross-section term in order to reproduce the observed spectra.

The single-photon expression given by Eq. (2) gives the correct form to reproduce the Ba^+ background if the spectral density of the $6p\epsilon l$ continuum is set to a constant value of 1. The overlap integral between the initial Rydberg state and the final continuum level does not have the functional form shown in Eq. (5). For a final state in the continuum, the overlap integral does not oscillate as the energy of the continuum level increases. Instead, the overlap integral consists of the same energy denominator given in Eq. (10) multiplied by the sine of a nearly energy-independent phase factor.

As shown by Bhatti *et al.* [25], the amplitude of the sine phase factor in the overlap integral between an initial and final Rydberg state is completely determined by the difference in the radial phases of the two wave functions at the origin. The phase factor in the overlap integral oscillates as the energy of the final state is changed because the radial phase of the final-state wave function at the origin changes. As the energy of a bound-state increases, the radial phase of wave function is fixed at the outer turning point and not at the inner turning point. Continuum waves, on the other hand, have a nearly constant radial phase at the origin. This phase changes extremely slowly with increasing energy due to the steep slope of the effective radial potential near the origin. Thus, the difference between the radial phase of the bound initial state and the continuum final state determines the amplitude of the excitation to the continuum. Unfortunately, the phase of the continuum wave, for the energy range in which we are interested, is not known for $6p\epsilon l$ levels so the amplitude of the background produced by excitation of the $6p\epsilon l$ continuum cannot be calculated.

Another problem with obtaining the amplitude of the Ba^+ background was discussed in the experimental section. The volume of atoms which experience a laser intensity great enough so that they may absorb a single photon is on the order of 20 times greater than the volume of atoms which are able to absorb two photons. Hence, we are unable to calculate the amplitude of the background from first principles. Therefore, in order to fit the single-photon background, we have used an arbitrary parameter C for the amplitude of the single-photon signal. The overlap integral is assumed to have the functional dependence described above for a continuum final state. Also, by virtue of the different peak amplitudes observed for single- and double-photon absorption, we assume that, at the third-laser frequency where the two-photon processes occur, the single-photon background comes predominantly from a region which is not depletion broadened.

The total number of ions we see per laser shot is

$$N=C\sigma\Phi+(1-e^{-\sigma_T\Phi})\ ,$$

where σ_T is given by Eq. (13) and σ is given by Eq. (2) with the modifications discussed above for the form of the overlap integral and the spectral density. Using this expression for N assumes that the total ion signal is simply a sum of the single- and two-photon contributions. The time-integrated photon flux Φ is estimated using laser power measurements and then varied slightly to give a good fit to the data. The variation of the values of Φ which fit the different data agrees well with the laser power variations.

In order to calculate the angular terms in the expressions for σ and σ'_T, we assume that the initial Rydberg states which we excite are true singlet $6snd\ ^1D_2$ levels. Although the resolution of the second laser was too poor to resolve the singlet and triplet levels for the highest-n states, we assume that the excitation of the triplet levels is negligible based on the relative amplitudes of the singlet and triplet states for the lower-n states. The angular integrals are then performed using the methods of Edmonds [28]. The MQDT parameters, which are used in the fit, are identical for the fine-structure components of the outer electron. The values used are

$$\delta_{6d_{3/2}nd_{3/2}}=3.08\ ,$$

$$\delta_{6d_{5/2}nd_{3/2}}=3.12\ ,$$

$$\delta_{6d_{5/2}nd_{5/2}}=3.12\ ,$$

$$\nu^3\Gamma_{6d_{3/2}nd_{3/2}}=0.17\ (\text{a.u.})\ ,$$

$$\nu^3\Gamma_{6d_{5/2}nd_{3/2}}=0.15\ (\text{a.u.})\ ,$$

$$\nu^3\Gamma_{6d_{5/2}nd_{5/2}}=0.15\ (\text{a.u.})\ ,$$

which are in excellent agreement with the experimental values.

Examples of the theoretical fits are shown as the solid curves in Figs. 3 and 4. Note that the only real discrepancy between the fits and the data occurs in the saturated scans shown in Fig. 3. Again, the explanation of these discrepancies lies in the nonuniformity of the laser beam and the excitation of different volumes at the peak of the cross section rather than in the wings.

ANALYSIS OF THE $6d_jnf_{j'}$ $J=5$ SERIES

In order to reproduce the $6d_{3/2}nf_{7/2}$, $J=5$ spectra, we use the same formulation used to reproduce the $6dnd$ data. In using this formulation, we neglect any interaction between channels converging to $6d_{3/2}$ and those converging to $6d_{5/2}$. Since, for the $6dnf$ and $6dng$ series we collected only electrons with energy greater than 1 eV, instead of ions, we observe no background signal due to excitation of the $6p\epsilon l$ continua. We still observe a very small energy-dependent background due to the partial

$6s\epsilon l'$ mixing with the $6p\epsilon l$ continua. In order to fit this baseline signal, we have used a background of arbitrary slope and amplitude. We have also assumed that the detuning parameters $\Delta_{j'}$ in Eq. (9) have a constant value of

$$\Delta_{j'}=E_{6s}-E_{6p_{j'}}+\tfrac{1}{2}(E_{6d_{3/2}}-E_{6s}) .$$

For the range of photon energies used in our experiments, this approximation leads to a maximum amplitude error of $\simeq 5\%$ in the wings of the observed features. We have also assumed that the laser frequency ω is constant over the energy ranges studied.

Typical cross-section measurements along with the energy-independent theoretical fit are shown in Fig. 12. The agreement between theory and experiment is excellent. The best-fit parameters obtained are

$$\delta_{6d_{3/2}nf_{7/2}}=0.97 ,$$

$$R'=0.67 ,$$

where R' and δ are the bound-continuum interaction parameter and quantum defects defined by Eq. (11).

For the $6d_{5/2}nf$ states, we are not able to use the two-channel model which was used for the $6d_{3/2}nf$ states. Instead, we use a four-channel (two bound and two continuum channels) QDT and a slightly modified version of Eq. (9) to express the final-state cross section. If we allow for channel mixings between states converging to the same ion limit, Eq. (9) becomes

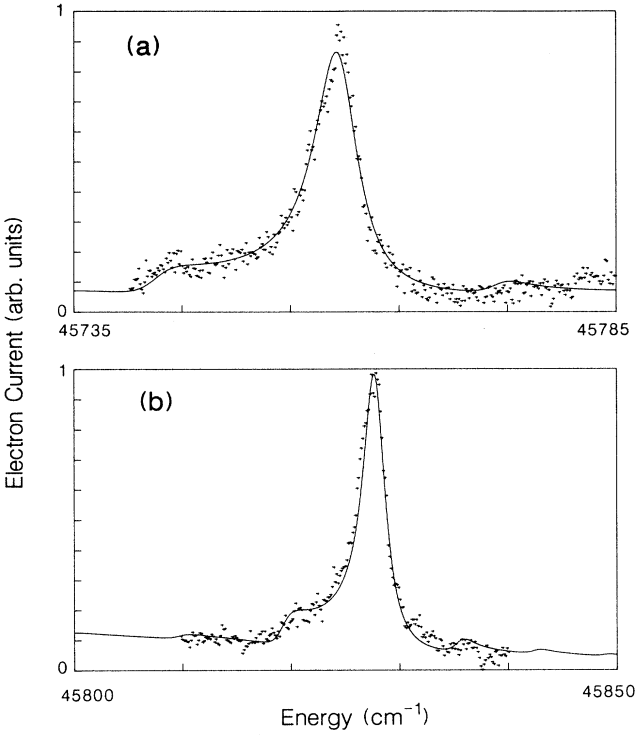

FIG. 12. Cross sections for excitation of the (a) $6d_{3/2}25f_{7/2}$, $J=5$ and (b) $6d_{3/2}31f_{7/2}$, $J=5$ states plotted as a function of final-state energy relative to the first ionization limit. The smooth curve is the result of the two-channel QDT fit to the data.

$$\sigma'=\frac{16\pi^3\omega^2\alpha^2\Phi}{\nu_i^3\tau}\sum_{k=1}^{n_c}\left|\sum_{j',j''}\frac{r_{6d_j 6p_{j'}}r_{6p_{j'}6s}}{\Delta_{j'}}\langle n'l'j''|nlj''\rangle A_k(n',l',j'')\right|^2 , \tag{14}$$

where $A_k(n',l',j'')$ is the spectral amplitude associated with the kth continuum, the bound channel where the state of the outer electron is described by the quantum numbers (n',l',j''), and n_c is the number of continuum channels (for this model $n_c=2$). Again the angular integrals are implicitly included in the radial matrix elements and overlap integrals and these were calculated using standard techniques [28]. Furthermore, we approximate

$$\Delta_{j'}=E_{6s_{1/2}}-E_{6p_{j'}}+\tfrac{1}{2}(6d_{5/2}-6s_{1/2})$$

for the range of photon energies studied.

The MQDT of Cooke and Cromer [27] was used to determine the spectral amplitudes. Since this procedure has been discussed in great detail in the literature [9,29] we will not discuss it further here. Instead, we simply report the set of parameters which best fit the experimental data. The collision channels which are used for the fit are

$$|\psi_1\rangle=|6d_{5/2}nf_{5/2}J=5\rangle ,$$

$$|\psi_2\rangle=|6d_{5/2}nf_{7/2}J=5\rangle ,$$

$$|\psi_3\rangle=|\mathscr{g}J=5\rangle ,$$

$$|\psi_4\rangle=|\mathscr{g}J=5\rangle ,$$

where $\mathscr{g}$ is the generalized continuum and the energy-independent R' matrix used to fit the data is

$$\underline{R}'=\begin{bmatrix} 0 & -0.015 & 0.654 & 0 \\ -0.015 & 0 & 0 & 0.470 \\ 0.654 & 0 & 0 & -0.365 \\ 0 & 0.470 & -0.365 & 0 \end{bmatrix} ,$$

$$\delta_1=\delta_{6d_{5/2}nf_{5/2}}=1.092 ,$$

$$\delta_2=\delta_{6d_{5/2}nf_{7/2}}=0.975 .$$

The results of the fit for two typical states are shown in Fig. 13. Note that the peak positions and widths of the calculated spectra agree quite well with the data. However, in Fig. 13(b) the relative amplitudes of the two features are not perfectly reproduced by the calculations. This discrepancy between theory and experiment is easily explained when we consider the character of the initial $6snf$ Rydberg state. As alluded to earlier in this work and as discussed in detail elsewhere, the $6snf$ series is strongly perturbed by the $5d8p$ and $5d4f$ configurations [19]. Due to these perturbations, a uniform classification of these levels in terms of LS or j-j coupling is not possible. In our analysis we have assumed that the initial Rydberg levels are good triplet states since the intermediate $5d6p\ ^3D_1$ and $6d5d\ ^3D_1$ levels are reasonably well described by LS coupling.

Previous analyses [9] have fit an additional rotation parameter in order to describe the initial Rydberg state as an arbitrary combination of j-j coupled channels. This procedure is quite reasonable if both members of the $6snf$ doublet for a given n can be excited. However, we have insufficient resolution to resolve the $6snf$ doublets, and therefore, fitting a rotation parameter to the initial Rydberg states would give little insight to the actual compositions of these states. The problem of improper classification of the initial Rydberg states becomes much more obvious when fitting the $6dng$ series which is discussed in the next section.

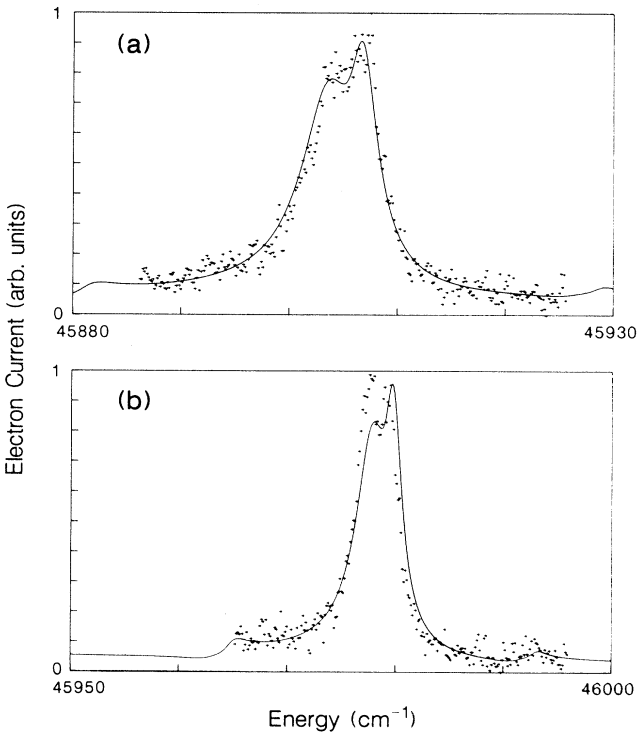

FIG. 13. Cross section for the excitation of the (a) $6d_{5/2}22f$, $J=5$ and (b) $6d_{5/2}26f$, $J=5$ series plotted as a function of final-state energy relative to the first ionization limit. The smooth curve is the result of the four-channel QDT fit to the data.

ANALYSIS OF THE $6d_jng_{j'}$ $J=6$ SERIES

As discussed briefly in the experimental section, the series converging to both fine-structure components of the Ba^+ $6d$ level are strongly perturbed. In order to reproduce the experimental spectra, we have used a ten-channel QDT model along with an expression for the observed cross section which is a slight modification of Eq. (14). Since we assume that the channels converging to the $6d_{3/2}$ limit interact with those converging to the $6d_{5/2}$ limit, we must also sum over the index j before squaring the amplitudes to different channels in Eq. (14).

Unfortunately, we were not able to reproduce the observed spectra using an energy-independent set of parameters. Therefore, the quantum defects and R' matrix parameters were allowed to vary linearly with the binding energy of the outer electron. The ten channels which were used in our model are labeled as

$$|\psi_1\rangle = |6d_{5/2}ng_{9/2}J=6\rangle ,$$
$$|\psi_2\rangle = |6d_{5/2}ng_{7/2}J=6\rangle ,$$
$$|\psi_3\rangle = |6d_{3/2}ng_{9/2}J=6\rangle ,$$
$$|\psi_4\rangle = |6d_{3/2}niJ=6\rangle ,$$
$$|\psi_5\rangle = |6d_{5/2}niJ=6\rangle ,$$
$$|\psi_6\rangle = |\mathcal{g}J=6\rangle ,$$
$$|\psi_7\rangle = |\mathcal{g}J=6\rangle ,$$
$$|\psi_8\rangle = |\mathcal{g}J=6\rangle ,$$
$$|\psi_9\rangle = |\mathcal{g}J=6\rangle ,$$
$$|\psi_{10}\rangle = |\mathcal{g}J=6\rangle .$$

Above the $6d_{3/2}$ ion limit, channels 3 and 4 become continua. Following the procedure outlined by Cooke and Cromer [27] the number of continua which are needed to describe the physical situation is equal to the number of bound channels. Therefore, above the $6d_{3/2}$ limit we consider only the three bound channels converging to $6d_{5/2}$ and three generalized continua. These continua are a simple rotation of the original continua and the two channels which converge to the $6d_{3/2}$ limit. Above this limit, the coupling of each bound channel to the continua is equal to the coupling of that channel to the original continua added in quadrature to the coupling with the $6d_{3/2}$ channels. Thus, above the $6d_{3/2}$ ion limit, only six channels are needed to reproduce the spectra.

Due to the size of the R' matrix used to calculate the spectral amplitudes, we split the R' matrix into four different parts. Following Cooke and Cromer we have,

$$\underline{R}' = \begin{bmatrix} \underline{R}'_{bb} & \underline{R}'_{bc} \\ \underline{R}'_{cb} & \underline{R}'_{cc} \end{bmatrix} ,$$

where $\underline{R}'_{bb}$, $\underline{R}'_{bc}$, $\underline{R}'_{cb}$, and $\underline{R}'_{cc}$ are all 5×5 matrices. Using this definition

$$\underline{R}'_{bb} = \begin{bmatrix} 0 & 0.03 & 0.28 & -0.15 & 0 \\ 0.03 & 0 & 0.10 & 0.15 & 33E \\ 0.28 & 0.10 & 0 & 0.07 & 0 \\ -0.15 & 0.15 & 0.07 & 0 & 0 \\ 0 & 33E & 0 & 0 & 0 \end{bmatrix},$$

where E is the magnitude of the binding energy of the Rydberg electron in atomic units. The matrix $\underline{R}'_{bc}$ is diagonal with elements

$$R'_{bc}(1,1)=0.41 ,$$

$$R'_{bc}(2,2)=0.20 ,$$

$$R'_{bc}(3,3)=87E+0.30 ,$$

$$R'_{bc}(4,4)=169E+0.04 ,$$

$$R'_{bc}(5,5)=0.10 ,$$

and $\underline{R}'_{cc}$ is identically zero. The quantum defects all have a marked energy dependence. We use

$$\delta_1=\delta_{6d_{5/2}ng_{9/2}}=-140E+0.334 ,$$

$$\delta_2=\delta_{6d_{5/2}ng_{7/2}}=-65E+0.368 ,$$

$$\delta_3=\delta_{6d_{3/2}ng_{9/2}}=-92E+0.333 ,$$

$$\delta_4=\delta_{6d_{3/2}ni}=-94E+0.354 ,$$

$$\delta_5=\delta_{6d_{5/2}ni}=-65E+0.356 .$$

Close inspection of Figs. 5(b), 6(a), and 7(a) clearly show that the experimentally determined quantum defects for the $6dnd$ and $6dnf$ series also have a noticeable energy variation.

The results of the calculations are shown in Fig. 8(b) and Figs. 9(b), 9(c), 10(b), and 10(c). Figures labeled (b) are reproductions of the spectra converging to the $6d_{5/2}$ ion limit [labeled (a)] and those labeled (c) should be compared to the $6d_{3/2}$ spectra in the figures denoted with (d). For states with $n>15$, the synthesized spectra are in good agreement with the observed data. In particular, the energy positions and widths of the features are in excellent agreement. Unfortunately, the relative intensities of all of the features are not correctly predicted by our model. As alluded to earlier, we attribute the discrepancies in the relative line strengths to improper classification of the initial $6sng$ levels as triplet states.

Consider the two spectra shown in Figs. 14(a) and 14(b). Figure 14(a) shows a calculation where the initial Rydberg level is taken to be $6s16g\ ^3G_4$. In this case, the ratio of the j-j coupled states $6s16g_{7/2}$ to $6s16g_{9/2}$ is $\sqrt{5}/2$. If this ratio is reduced to $\sqrt{5}/4$, the relative line strengths of the final state changes so that we would observe the spectra shown in Fig. 14(b). Clearly, this choice of rotation angle for the initial state yields a fit which resembles the data quite well. As is the case with the $6snf$ states, however, little information is gained by introducing a new rotation parameter for each initial state in order to achieve the best fit without any *a priori* knowledge of the true rotation angles. Therefore, the spectra shown in Figs. 8–10 all assume good triplet initial states.

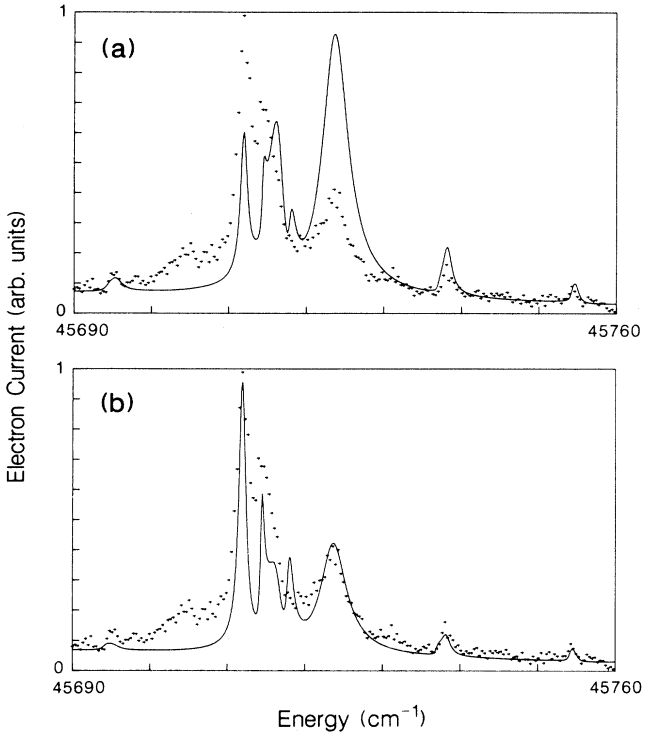

FIG. 14. Experimental and synthesized cross section for excitation of the $6d_{5/2}16g$ state. In (a) the calculation assumes a $6sng\ ^3G_4$ initial state with an amplitude ratio of $6sng_{7/2}$ to $6sng_{9/2}$ of $\sqrt{5}/2$, and in (b) the ratio of $6sng_{7/2}$ to $6sng_{9/2}$ in the initial state is taken as $\sqrt{5}/4$.

In Fig. 8(b) the synthesized spectra with principle quantum number $n>21$ are generated using the six-channel model which is only strictly appropriate for levels which lie above the $6d_{3/2}$ limit. The $6d_{3/2}$ limit is actually located on the high-energy side of the $6d_{5/2}23g$ level. However, due to the fact that our laser linewidth is large compared to the widths and energy spacings of the degenerate members of the $6d_{3/2}nl$ states above $6d_{5/2}21g$, the spectra we observe should be nearly identical to those calculated using the six-channel model. Inspection of Fig. 8 shows that this is, in fact, the case. Also, we note that many of the sharp features in the theoretical spectra for $n\leq 21$ are instrumentally broadened or washed out in the data.

Close inspection of the $6d_{5/2}$ spectra in Fig. 8(a) shows that there is an extra feature on the high-energy side of the main profiles for $n\geq 25$ which is not reproduced by the theory in Fig. 8(b). These features are believed to be $6dnd$ $J=5$ states, which are being excited from $6snd$ $J=3$ Rydberg levels. This assignment is made by comparing the quantum defects of the observed levels with the previously measured values for the $6dnd$ states. Our laser excitation scheme prevents excitation of these $J=3$ levels if our laser polarizations are 100% pure, so a possible explanation for the appearance of these extra features is nonperfect circular polarization. Another probable

cause for the imperfect angular-momentum selection in the final states stems from the possibility that, in the second step of our laser excitation scheme, the $5d6p\ ^3D_1$ level spontaneously decays to the $6s5d\ ^3D_2$ state instead of undergoing stimulated emission. We have found that the $5d6p\ ^3D_1$ level decays with nearly 100% probability to the $6s5d$ configuration in a time which is comparable to our laser pulse width of $\simeq 8$ ns. Thus, there is always some population in the metastable state which does not have the expected $M=2$ total angular-momentum projection. In any case, we ignore this complication in all of the synthesized spectra.

The theoretical spectra in Figs. 10(b) and 10(c) clearly do not reproduce the data as well as those in Figs. 8 and 9. The sharp features labeled A and B in Figs. 10(a) and 10(d) are believed to be even-parity $4fnl$, $J=6$ perturbers. These perturbers are also believed to be the source of the energy dependence of the R' matrix parameters and quantum defects of the $6dng$ series. Two other sharp features have also been observed near the $6d_{5/2}12g$ levels and near the $6d_{3/2}13g$ state. Recently, we have observed strong interactions between the $6dnf$ and $6dnh$ $J=3$ series and the $4fn'g$ states for $n'\leq 7$. In fact, we believe that $4fnl$ configurations are responsible for the energy dependence of the quantum defects for all of the $6dnl$ series observed. Observation and analyses of the $4fnl$ series are necessary in order to confirm this hypothesis, but preliminary work in this area seems to support our explanation.

CONCLUSIONS

We have studied the $6dnl$ autoionizing series in detail for $l=2$, 3, and 4 and have also observed several members of the $6dns$ series. The spectra we have acquired exhibit vastly different levels of interseries interaction. The $6dns$ and $6dng$ series show extremely large configuration interactions yet the $6dnd$ and $6dnf$ show little or no interseries interferences.

The $6dnd$, $J=4$; $6dnf$, $J=5$; and $6dng$, $J=6$ series have been fit using two-, four-, and ten-channel QDT models which reproduce the observed spectra very well. The only real discrepancies between the synthesized and experimental spectra are the relative amplitudes between different features in some of the scans. These differences are attributed to inappropriate labeling of the $6snf$ and $6sng$ Rydberg series in terms of LS coupling.

The $6dnl$ states for $l\geq 6$ have also been observed recently [30] using a Stark switching approach similar to the one used to populate the high-l $6pnl$ states [10]. Therefore, upon the completion of the analysis of the character of these states, the $6pnl$ and $6dnl$ series will be well understood. Over the past two years, experiments have been performed which use real autoionizing states as intermediate levels in order to reach higher core states. Specifically, we have used the $6pnl$ and $8snl$ states [31] while others have also used $6dnl$ and $6fnl$ [32] intermediate levels.

The results of this experiment clearly show that the character of the intermediate states in the excitation of higher-lying states is critical in determining the structure of the cross section for the excitation of the final states. The information about the $6dnl$ states obtained from this work is, therefore, extremely important when considering excitations through $6dnl$ intermediate states. Thus, although the experimental observation of even higher-lying states is an interesting and intriguing problem, understanding the composition of the lower-lying doubly excited states is a necessary prerequisite.

ACKNOWLEDGMENTS

We would like to acknowledge M. C. Baruch, L. T. Cai, and C. J. Dai for their assistance in some of the data acquisition. This work has been supported by the National Science Foundation under Grant No. PHY 9001126.

[1] W. E. Cooke, T. F. Gallagher, S. A. Edelstein, and R. M. Hill, Phys. Rev. Lett. **40**, 178 (1978).
[2] F. Gounand, T. F. Gallagher, W. Sandner, K. A. Safinya, and R. Kachru, Phys. Rev. A **27**, 1925 (1983).
[3] N. H. Tran, P. Pillet, R. Kachru, and T. F. Gallagher, Phys. Rev. A **29**, 2640 (1984).
[4] S. M. Jaffe, R. Kachru, H. B. van Linden van den Heuvell, and T. F. Gallagher, Phys. Rev. A **32**, 1480 (1985).
[5] E. Y. Xu, Y. Zhu, O. C. Mullins, and T. F. Gallagher, Phys. Rev. A **33**, 2401 (1986).
[6] P. Camus, P. Pillet, and J. Boulmer, J. Phys. B **18**, L481 (1984).
[7] L. A. Bloomfield, R. R. Freeman, W. E. Cooke, and J. Bokor, Phys. Rev. Lett. **53**, 2234 (1984).
[8] N. Morita, T. Suzuki, and K. Sato, Phys. Rev. A **38**, 551 (1988).
[9] R. R. Jones, C. J. Dai, and T. F. Gallagher, Phys. Rev. A **41**, 316 (1990).
[10] R. R. Jones and T. F. Gallagher, Phys. Rev. A **38**, 2846 (1988).
[11] P. Camus, M. Dieulin, A. El Himdy, and M. Aymar, Phys. Scr. **27**, 125 (1983).
[12] E. A. J. M. Bente and W. Hogervorst, Phys. Rev. A **36**, 4081 (1987).
[13] E. A. J. M. Bente, Ph.D. thesis, Vrije University, Amsterdam, 1989.
[14] R. Kachru, N. H. Tran, H. B. van Linden van den Heuvell, and T. F. Gallagher, Phys. Rev. A **30**, 667 (1984).
[15] T. W. Hansch, Appl. Opt. **11**, 895 (1972).
[16] M. Aymar, P. Camus, M. Dieulin, and C. Morillon, Phys. Rev. A **18**, 2173 (1978).
[17] M. Aymar and O. Robaux, J. Phys. B **12**, 531 (1979).
[18] C. E. Moore, *Atomic Energy Levels,* Natl. Bur. Stand. (U.S.) Circ. No. 467 (U.S. GPO, Washington, DC, 1949),

Vol. 3.
[19] B. H. Post, W. Vassen, W. Hogervorst, M. Aymar, and O. Robaux, J. Phys. B **18**, 187 (1985).
[20] P. Camus, M. Dieulin, and A. El Himdy, Phys. Rev. A **26**, 379 (1982).
[21] W. E. Cooke, S. A. Bhatti, and C. L. Cromer, Opt. Lett. **7**, 69 (1982).
[22] C. J. Dai, G. W. Schinn, and T. F. Gallagher, Phys. Rev. A **42**, 223 (1990).
[23] M. Aymar and J.-M. Lecomte, Phys. B **22**, 223 (1989).
[24] E. Merzbacher, *Quantum Mechanics,* 2nd ed. (Wiley, New York, 1970); L. I. Schiff, *Quantum Mechanics,* 2nd ed. (McGraw-Hill, New York, 1955).
[25] S. A. Bhatti, C. L. Cromer, and W. E. Cooke, Phys. Rev. A **24**, 161 (1981).
[26] W. E. Cooke and C. L. Cromer, Phys. Rev. A **33**, 3529 (1986).
[27] W. E. Cooke and C. L. Cromer, Phys. Rev. A **32**, 2725 (1985).
[28] A. R. Edmonds, *Angular Momentum in Quantum Mechanics* (Princeton University, Princeton, 1960).
[29] C. J. Dai, S. M. Jaffe, and T. F. Gallagher, J. Opt. Soc. Am. B **6**, 1486 (1989).
[30] P. Camus (private communication).
[31] R. R. Jones and T. F. Gallagher, Phys. Rev. A **42**, 2655 (1990).
[32] U. Eichmann, V. Lange, and W. Sandner, Phys. Rev. Lett. **64**, 274 (1990).